



Reactivity Controlled Compression Ignition combustion and emissions using *n*-butanol and methyl oleate

Valentin Soloiu*, Jose D. Moncada, Remi Gaubert, Aliyah Knowles, Gustavo Molina, Marcel Ilie, Spencer Harp, Justin T. Wiley

Department of Mechanical Engineering, Georgia Southern University, Statesboro, GA 30460, USA



ARTICLE INFO

Article history:

Received 5 May 2018

Received in revised form

13 August 2018

Accepted 27 September 2018

Available online 28 September 2018

Keywords:

Reactivity controlled compression ignition

Low temperature combustion

Combustion

Methyl oleate

Biodiesel surrogate

n-Butanol

ABSTRACT

Direct Injection of methyl oleate and PFI of *n*-butanol were used to conduct Reactivity Controlled Compression Ignition (RCCI) and minimize exhaust emissions in reference to conventional diesel combustion. Methyl oleate was investigated for validation of a single fatty acid methyl ester as a surrogate for biodiesel in engine operation. An experimental common rail engine was operated in RCCI and conventional diesel combustion modes under constant boost and similar combustion phasing. The RCCI strategy used two pulses of direct injections with a fixed first injection at 60° before top dead center and a varied second injection for smooth combustion. Ringing intensity was reduced by 70% for methyl oleate RCCI compared to diesel conventional diesel combustion. The molecular oxygen from methyl oleate allowed a reduction in soot by 75% and 25% compared to diesel in RCCI and conventional diesel combustion operation, respectively. Compared to conventional diesel combustion, NOx and soot decreased for RCCI by several orders of magnitude with both emissions approaching near zero levels at low load. The fuels produced a stable RCCI operation where mechanical efficiency was sustained within 2% for same-load points and the coefficient of variation of indicated mean effective pressure was limited to 2.5%.

Published by Elsevier Ltd.

1. Introduction

Diesel engines are essential in modern transportation and power supply applications; however, they can cause harmful exhaust emissions. Common emissions control is achieved through exhaust after treatment systems which tend to be expensive requiring extensive calibration. As an alternative, advanced combustion modes have been developed to rather control the in-cylinder emissions formation through low temperature combustion (LTC). Most prevalent methods to achieve LTC can be recognized as homogenous charge compression ignition (HCCI), premixed charge compression ignition (PCCI), and reactivity-controlled compression ignition (RCCI). HCCI lacks control of ignition timing, tending to autoignite prematurely due to high mixing rates early in the combustion cycle, inducing high maximum pressure rise rates (PPRR) and knock [1,2].

PCCI addresses early ignition through control of early injection [3], however, conventional PCCI achieves increased ignition delay

with high rates of exhaust gas recirculation (EGR), resulting in lower combustion efficiencies under 90% at medium-high loads and can suffer from increased emissions from wall wetting [4]. Using different fuel reactivity was thus introduced in conjunction with variable injection to achieve stratified ignitability [5]. RCCI was thus developed to change the chemical kinetics for emissions control improving the regulation of the heat release and lower exhaust gas recirculation (EGR) rates; the load range can be expanded with RCCI reaching loads unattainable with HCCI or PCCI [6]. In addition to concern in emissions, the transportation sector deals with a substantial demand on foreign oil supply [7]. In this study, RCCI is thus investigated with the use of renewable biofuels due to the limited sources of petroleum diesel and to promote energy security. The effects of biodiesel on LTC strategies, such as RCCI, are still under investigation in literature.

RCCI can be described as an advanced injection strategy that utilizes fuels of different reactivities to achieve a reactivity and equivalence ratio stratification across the cylinder [8,9]. The low reactivity fuel is delivered through early port fuel injection while a high reactivity fuel is delivered into the cylinders at higher pressures through common rail operation in either a single or dual pulse. The injection strategy achieves low temperature heat release

* Corresponding author.

E-mail address: vsoloiu@georgiasouthern.edu (V. Soloiu).

and variable local ignition delay to eliminate rich and non-homogenous zones as well as reduce combustion temperatures, effectively reducing NO_x and soot simultaneously. RCCI has been conducted with PFI of gasoline and DI of diesel, sweeping intake temperatures and injection timing with constant combustion phasing through variable fuel ratios. NO_x emissions were able to be reduced by 30% and soot by 90%, however, CO emissions increased by several orders when compared to conventional diesel combustion (CDC). Combustion efficiency for RCCI ranged from 90% to 97% with increasing load, while CDC resulted in an efficiency of 97%–99% [10].

In terms of PFI, renewable ethanol and methanol have been used to replace gasoline as the low reactivity fuel in RCCI. E85 has been investigated in comparison to gasoline across loads when operated with ULSD#2 [11]. The use of E85, which had a higher octane number than UTG-96, expanded the load range of RCCI for a light-duty experimental engine. The ratio of premixed to direct injected fuel was lower by up to 20% and the SOI was retarded by 5 CAD for E85 operation. The alcohol was assumed to delay the low temperature ignition, having an intake cooling effect, which allowed for further use of diesel and reduced UHC emissions and increased BTE at high load conditions. Fuel consumption decreased at higher load points for E85 compared to ULSD in an equivalent gram basis [12]. Neat ethanol along with methanol was approached similarly as a low reactivity fuel through different loads in a numerical study [13]. A higher diesel fraction was required for ethanol and methanol operation to sustain combustion phasing when compared to gasoline PFI, which related to the lower reactivity of these alcohols. At lower load conditions, the operating points were more sensitive on the diesel DI, where NO_x and soot were higher for methanol and ethanol PFI. This behavior additionally led to faster pressure rise for the alcohols. On the other hand, at high load, soot was more affected by the oxygen content of the alcohols and due to a lower difference in DI mass between the tested low reactivity fuels.

In this study, normal butanol was selected as the PFI as it has a higher calorific value than ethanol and can be produced from common sources [14]. It additionally has very good solubility with ULSD, showing no phase separation after blended [15]. n-Butanol has been used neat and in fuel blends for conducting conventional to premixed combustion modes and reducing overall emissions [16,17]. There is, however, a literature gap in n-butanol evaluation along with renewable high reactivity fuels such as biodiesel in RCCI operation. Several studies of neat biodiesel have been conducted as a result of directives relating to the EPA regulations, which require higher volumes of fuel produced from biomass to be available nationwide [18]. Various biodiesels from different feedstocks have been investigated in CI engines [19] where the majority of literature can be summarized as improved soot and carbon dioxide emissions as well as higher combustion efficiency using biodiesel compared to CDC [20]. In addition, biofuel has been characterized as biodegradable and nontoxic with the ability to be used with little to no modification in diesel engines and maintain similar performance to ULSD#2 [21]. Nonetheless, biodiesel quality of any biomass was also found important for outlining its long-term effects on engine performance and emissions reduction [22].

The advantages found in biodiesel operation can then be beneficial for advanced strategies such as RCCI. Each biodiesel, however, is different due to each possessing a diverse fatty acid methyl ester (FAME) profile. This characteristic has allowed for studies looking for prediction in the performance of a biofuel based on their FAME profile. In the effort to simplify the use of biodiesel and its combustion characteristics, a predominantly single FAME was analyzed in this study as a viable surrogate. Methyl oleate (MO) was selected and, like n-butanol, is renewable and can be produced from non-edible feedstock and agricultural byproducts or waste

[23,24]. MO is one of the main FAMEs that compose biodiesel among others such as stearic, linoleic, linolenic, and palmitic acid. It presents a favorable cetane number in contrast to the lower reactivity linoleic and linolenic methyl esters [25] and can be inferred as the backbone of some biodiesel [26].

The effect of methyl oleate on combustion has been previously investigated in respect to its composition in a biodiesel mixture. Palm oil methyl ester (PME) blends with methyl oleate were investigated in a single-cylinder DI engine. The palm biodiesel was enriched with methyl oleate and achieved lower soot emissions as well improved BSFC. This can be related to the lower oxygen concentration and lower reactivity of neat PME. Further, the results supported that increased saturated methyl esters led to lower exhaust gas temperature and emissions while sacrificing fuel consumption [27]. The addition of methyl esters was explored similarly for alcohol-diesel blends in an engine operating at low-medium load with low boost and rates of EGR. It was noted that the use of 15% FAME was sufficient to meet lubricity standards and prevent phase separation of the blends. The unsaturation degree of methyl oleate was beneficial for reducing UHC and CO in comparison to methyl stearate and methyl esters with similar carbon chain. Similar soot levels and lower NO_x concentrations were obtained for C18:1 in comparison to rapeseed biodiesel [28]. Soloiu et al. [29] investigated an equal-parts blend of methyl oleate and diesel in a mechanically injected direct injection engine at various speeds. The methyl oleate blend decreased the ignition delay by 20% compared to ULSD baseline, decreasing peak pressures and peak gross heat release. NO_x decreased by 20% compared to diesel while combustion efficiencies were maintained. BSFC increased by around 10% across speeds for the methyl oleate blend due to lower energy content. The use of methyl oleate was similarly explored in an indirect injection engine and identified as a performance improver [30].

MO has not been investigated for a common rail direct injection engine in LTC. Moreover, methyl oleate has not been studied in dual fuel strategies and n-butanol has not been investigated when coupled with neat fatty acid methyl esters (FAME) for RCCI operation. Additionally, 100% FAME has not been investigated as a full replacement for petroleum diesel in RCCI, moreover much remains unknown about the impact of higher pressures, premixed ratios, and multifuel mixtures on this strategy. Combustion efficiency has been initially investigated with 20% soy FAME blend in RCCI mode and showed improvements at low loads [31]. Introducing FAME into the combustion strategy allowed control of the two-stage heat release without increasing the PFI fraction to the extent required with ULSD. The purpose of this study was to then expand on the FAME and high fuel reactivity literature [32] and determine if methyl oleate is a viable surrogate to biodiesel in RCCI operation, thereby facilitating the biodiesel use in dual fuel combustion.

2. Physiochemical properties of selected fuels

2.1. Fuel characteristics

Physiochemical properties of the fuels were investigated as they influence the atomization, mixture formation, and emissions characteristics of an engine. Table 1 summarizes the results for selected fuel properties analyses done by the authors. The flash point for the fuels, referring to the minimum temperature at which the vapors will ignite, were found from literature for ULSD and n-butanol while the methyl oleate flash point was obtained from the supplier. A 1341 Parr constant-volume oxygen (25 atm) calorimeter was used to determine the energy content of the fuels with lower heating value (LHV). The calculated LHV can be correlated to the heat released in the cylinder which can affect the fuel consumption.

Table 1
Selected fuel properties.

	ULSD#2	Methyl Oleate	n-Butanol
DCN ^a	47	68	16
ID from CID 510 ^a	3.47 ms	2.49 ms	40.2 ms
Density ^a	0.836 g/cm ³	0.876 g/cm ³	0.807 g/cm ³
Viscosity @ 40 °C ^a	2.52 cP	4.54 cP	2.04 cP
Lower Heating Value ^a	42.6 MJ/kg	37.0 MJ/kg	33.1 MJ/kg
Flash Point**	53.5 °C min	163 °C	35 °C

^a Determined in this study; **found in literature [35].

FAME was determined to have a 13% lower energy density than diesel.

A Brookfield DV II Pro rotational viscometer set at 200 RPM spindle speed was used to determine the dynamic viscosity of the fuels for a temperature range of 26–90 °C. Viscosity was measured due to its effect on the spray droplet diameter and rate of vaporization. Increased viscosity can cause poor atomization which leads to production of particulate matter and deposits in the injection system while lower viscosity can accelerate the wear on the injector given decreased lubricity. Biodiesel can help attain enhanced injector plunger efficiency with its common higher lubricity, even used as an additive for other fuels, although it can result in cold flow problems due to its high viscosity [33]. n-Butanol viscosity is relatively close to diesel than other alternatives like kerosene [34]. As shown in the fuel properties table and illustrated in Fig. 1, methyl oleate viscosity is close to double of that of diesel at 40 °C. This relates to the higher number of saturated carbons in the molecular structure of the FAME as well as the overall molecular mass. The higher viscosity comes with high lubricity for the FAME, however, which can reduce friction losses at standard atmospheric conditions. Similar droplet sizes can then be obtained in-cylinder if a homogenous mixture is achieved with FAME and n-butanol, compensating for the atomization of methyl oleate.

A constant volume combustion chamber (CVCC)-PAC CID510 was used to determine the derived cetane number (DCN). The ignition delay (ID) of n-butanol was found to be ten times higher

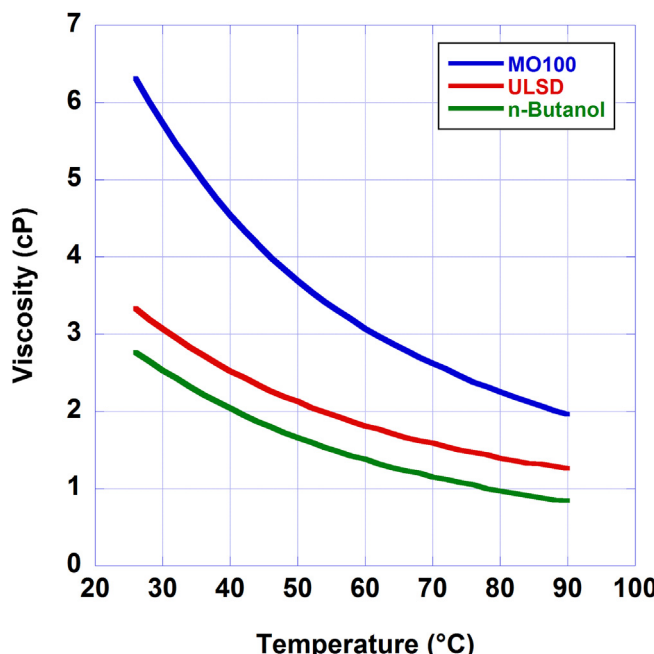


Fig. 1. Fuel dynamic viscosity from 26 °C to 90 °C.

than ULSD#2, showing the great difference in reactivity as seen in Fig. 4. A CAD model of the CVCC is shown in Fig. 2, which illustrates (1) the electronic fuel injection system with pressure multiplier, (2) the uniformly heated test chamber, (3) the chamber pressure sensor, and (4) the injection pressure sensor. The injection system implemented a Bosch common rail injector with 6 × 0.17 mm nozzle holes [36]. The DCN was calculated using Equation (1) which employs values for ID and combustion delay (CD) of the fuel as determined from the combustion in the chamber following ASTM standard [37]. The ID is defined as the period between the leading edge of the electronic pulse sent to the common rail injector and when the chamber pressure reached 0.02 MPa above the static pressure. The CD is similarly defined as the period between the leading edge of the electronic pulse sent to the common rail injector and the middle of the combustion pressure curve. These variables were measured from the average of 15 injection cycles per run in the CVCC. Each cycle contains a fresh charge of air at the set equilibrium temperature for 3 runs for each fuel. The fuel was delivered to the chamber, which was pressurized at 20 bar and uniformly heated at 595 °C, with a 1000 bar rail pressure and 2.5 ms injection duration.

$$DCN = 13.028 - \frac{5.3378}{ID} + \frac{300.18}{CD} - \frac{1267.90}{CD^2} + \frac{3415.32}{CD^3} \quad (1)$$

The results from CVCC shows that the fuels have characteristic reaction pathways that inherently compound with the chemical composition to generate different pollutant species and heat release patterns. As observed in Fig. 3, the pressures increased as the ignition delay increased until a threshold was reached. Neat ULSD#2 attained a pressure of 42 bars while methyl oleate reached a maximum pressure of 39 bars. The higher reactivity of the FAME led to less premixing and limited the peak combustion pressure compared to ULSD#2. The heat release rates, illustrated in Fig. 4, were dependent to the pressure rise rate due to the constant volume [36].

Before the start of pressure rise for n-butanol, the curve can be observed to decrease the pressure in the chamber below 20 bars due to the high latent heat of vaporization that is characteristic of this alcohol. The resulting combustion is smoother for n-butanol as observed with low peak heat release rate. The relative air fuel ratio is additionally larger for n-butanol, correlating to a leaner cycle. The late combustion is desired, however, for conducting RCCI, which averts early ignition that can result in high COV of IMEP and knock due to combustion phasing close to TDC. The maximum heat release rate was 95% lower for n-butanol than ULSD#2. The heat release rates (AHRR) of the neat fuels also result in ringing in the chamber; remaining fuel keeps reacting with surrounding air after

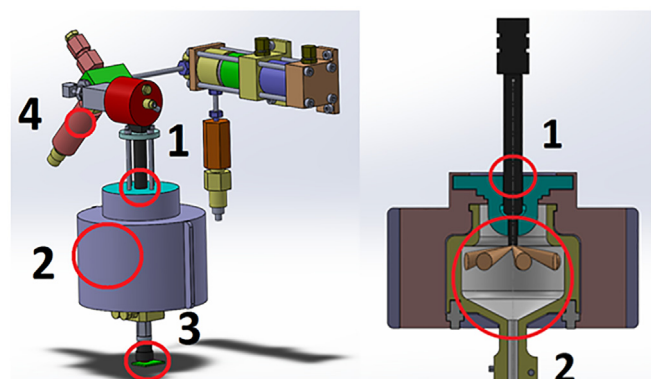


Fig. 2. CVCC main instrumentation.

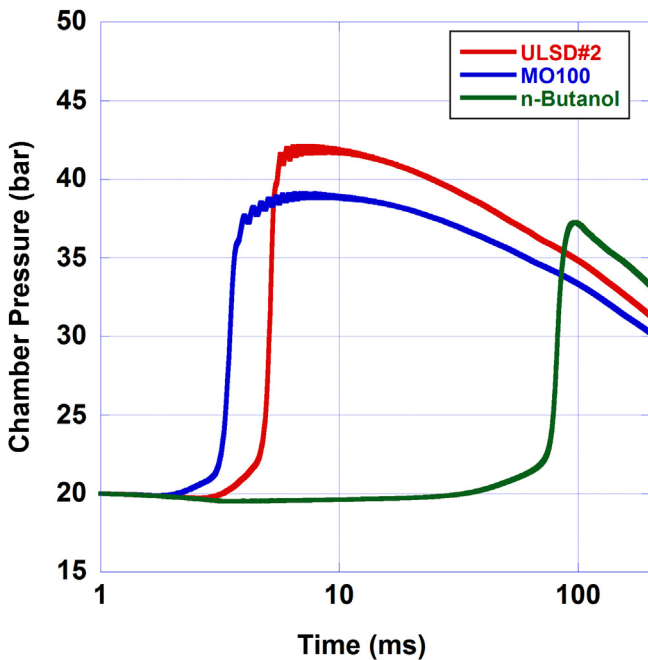


Fig. 3. Pressure for studied fuels in the CVCC.

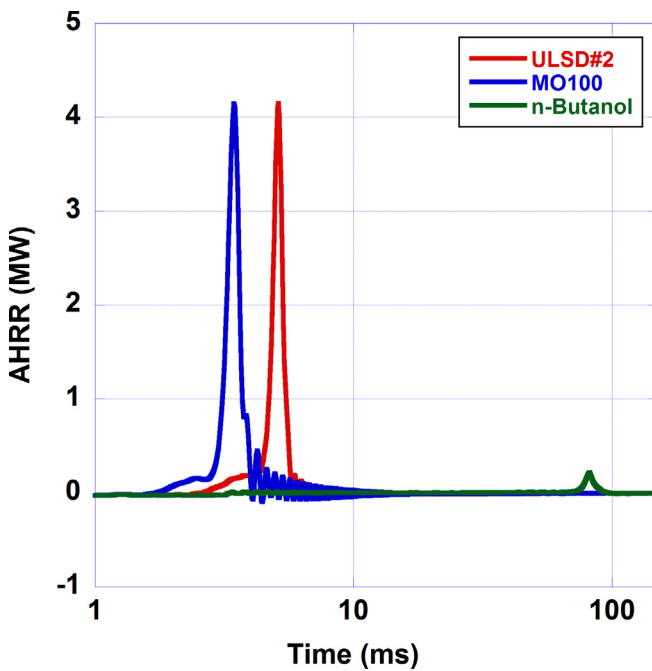


Fig. 4. Heat release rate for studied fuels in the CVCC.

ignition. This behavior is not encountered in the alcohol due to the longer mixing time before the combustion, which led to increased air utilization and limited high energy release. A closer view of the AHRR is shown in Fig. 5, displaying the negative temperature coefficient (NTC) region in detail.

The AHRR suggest that the fuels exhibit unique reaction pathways and rates, depending on their chemical composition, physical properties, and the pressure and temperature in the combustion chamber and consequently have different ignition delays, heat release patterns, combustion phasing, pollutant species, and

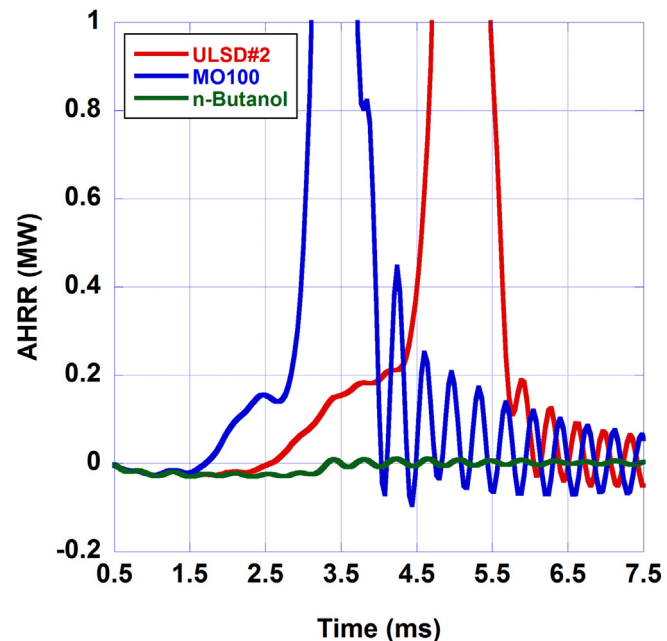


Fig. 5. LTHR and NTC detail in the CVCC.

concentrations in the combustion system. Methyl Oleate (MO100) had a more prominent NTC region than ULSD#2, however where ULSD#2 lacked an NTC the low temperature heat release region had a longer duration. The NTC region is the negative slope of the low temperature heat release where the low temperature combustion slows for a small period of time. The NTC region increased slightly due to its strong fuel ignition reactivity in MO100. Strong ignition reactivity and slight NTC behavior produced the fast reaction rate and fuel consumption observed for MO100.

2.2. Low temperature heat release analysis by TGA-DTA

Each fuel must attain a characteristic temperature before it vaporizes and allows further mixing. For this effect, a thermogravimetric analysis and differential thermal analysis (TGA-DTA) was used to measure vaporization and energy release characteristics of the tested fuels. Both analyzes were achieved when using a Shimadzu DTG-60 apparatus which sets fuels samples in a constantly purged air atmosphere (5 mL/min). Fuel samples are placed in aluminum pans and heated up to 600 °C at a rate 20 °C/min. The fuel sample was tested with an inert reference, usually alumina, which loses little to no mass.

Thermal fuel behavior was analyzed with the TGA curve as observed in Fig. 6, illustrating the vaporization of the neat fuels investigated. TGA fundamentally indicated at what temperatures 10%, 50%, and 90% of the sample mass has been vaporized (TA10, TA50, and TA90, respectively), as provided in Table 2. A higher vaporization rate would potentially decrease spray penetration in the combustion chamber. Vaporization rates and behavior of each fuel can be observed in the TGA curve. MO100 started vaporization at a higher temperature, yet, it vaporized at a faster rate than ULSD#2, reaching a similar TA90 as the diesel. This could be related to the oxygen content in the fuel facilitating the initial oxidation as well as the unsaturated characteristic of C18:1. n-Butanol was almost completely vaporized at 100 °C.

The DTA represented the fuel energy from low temperature heat release in an environment with rising temperatures. This correlates well to the cylinder at the end of the compression stroke. DTA

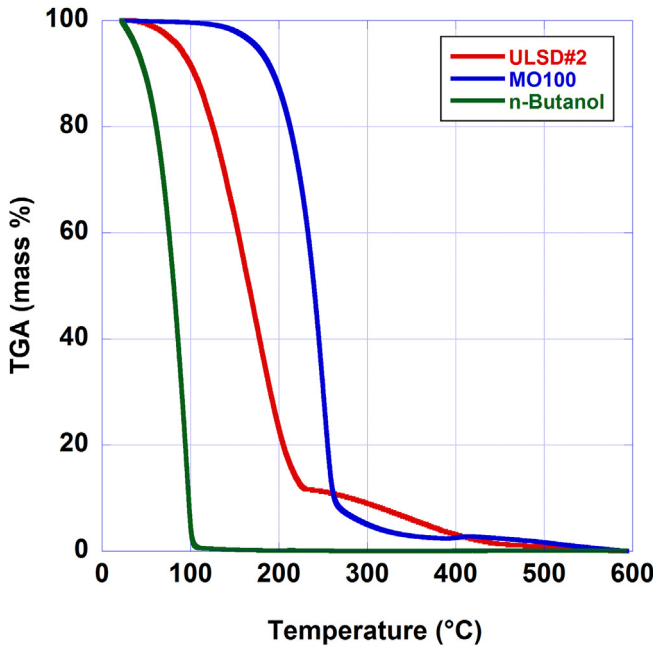


Fig. 6. TGA for selected fuels.

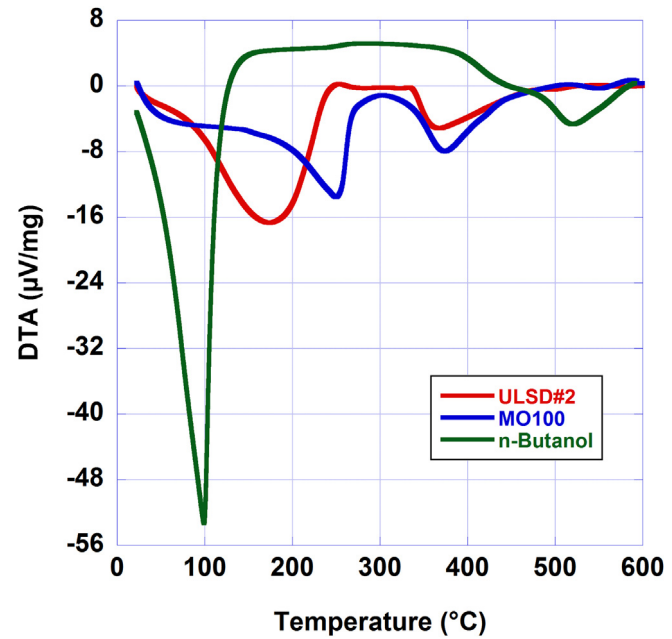


Fig. 7. DTA for selected fuels.

Table 2
Vaporization temperatures.

	ULSD#2	MO100	n-Butanol
TA10	105 °C	200 °C	45 °C
TA50	165 °C	245 °C	80 °C
TA90	280 °C	275 °C	95 °C

shows specific changes in micro voltage for thermocouples placed around the sample and the baseline; the voltage will vary accordingly to the heat required and released by the fuel. The curve indicates when the fuel undergoes exothermic and endothermic reactions by its convex and concave points, respectively. The DTA can additionally show two-stage energy release consisting of oxidation and pyrolysis. This is useful for biodiesel as each fuel has a different FAME composition with different thermal behaviors. The energy release profile is displayed in Fig. 7 for all the fuels. A high endothermic reaction can be observed for n-butanol due to its latent heat of vaporization [38], peaking at almost its complete vaporization. This correlated with the high temperature detected in the DTA as a continuously higher peak until 400 °C.

2.3. Mie scattering spray analysis

Combustion characteristics are heavily affected by spray development and mixture formation. Spray development was studied using a Malvern Mie scattering 10 mm diameter with a wavelength 632.8 nm. Helium-Neon laser with Spraytec software. As seen in Fig. 8, the laser light (1) is set into an accurately wide parallel beam by the optics (2). The spray droplets scatter the light from the laser (3). Focusing lens adjust the scattered light (4) in a Fourier arrangement and registered by the detector array (5). A reference injector from the research engine was used to inject into the atmospheric air and temperature (297 K). Data was captured at 10 kHz for 3 ms after triggering the injection. Injection parameters were identical between experiments with different fuels to serve as a comparative study of atomization regimes. The laser system was, however, not configured for replication of ambient conditions in

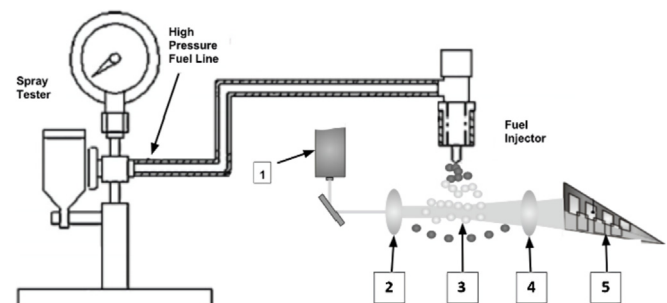


Fig. 8. Data capture for the Spraytec software.

the cylinder.

Refractive indices were estimated for the fuel binary mixtures. The detected droplet sizes will vary across the spray structure; air mixing will be dependent on the diameter distribution at its core as the edges are the first to vaporize. Sauter Mean Diameter was determined for the tested fuels as droplet diameter will affect combustion efficiency due to different effective surface area. The SMD determination stemmed from the British Standard BS2955:1993. Spray volume distribution was additionally determined by averaging the range of collected data. Uneven droplet distribution can result in unburned carbon emissions.

The spray droplet diameter over time and SMD are illustrated in Fig. 9 for the high reactivity fuels, as the fuels were delivered by the same injector. Peak spray volume frequency was at 34 μm for ULSD#2 and at 40 μm for MO100. A shift toward larger droplets can be observed for the methyl oleate as well as a higher peak overall; the SMD was continuously higher for the FAME, correlating to its viscosity. The SMD difference is smaller over time as more of the spray core is detected by the laser. The average SMD were determined as 22.8 μm for ULSD#2 and 27.5 μm for MO100. Table 3 includes the droplet sizes below which 10%, 50%, and 90% of the total spray volume lies and the percent of the spray volume under 10 μm. These values help explain the shift in volume frequency seen in the spray distribution curves. The maximum difference in spray

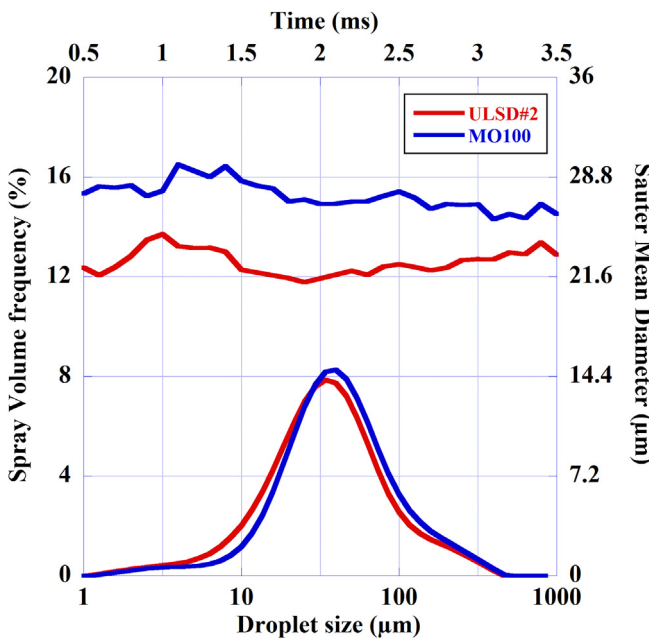


Fig. 9. Spray volume distribution for selected fuels.

Table 3
Spray droplet size by volume (μm).

(μm)	D _v (10)	D _v (50)	D _v (90)	%v < 10 μm
ULSD#2	12.3	37.9	120.5	9.5%
MO100	16.0	43.4	134.1	5.8%

numbers between the fuels becomes larger as the whole spray volume is considered. Injection of the biodiesel surrogate will help sustain further penetration into the cylinder when combined with the higher thermal stability of the methyl ester.

3. Experimental methods

3.1. Experimental Engine Setup

Methyl oleate performance was investigated in a single-cylinder, experimental CI engine in both RCCI and conventional combustion modes and in comparison to a ULSD#2 reference at 1500 RPM (near maximum brake torque) and constant load sweep. The studied load range was set at 4–6 bars indicated mean effective pressure (IMEP) in order to explore the low-medium load of the experimental engine. The engine was connected to a hydraulic dynamometer to simulate the resistive load measured with a TQ513 torque cell (accuracy $\pm 0.10\%$, standard error (SE) 0.06%). The experimental engine specifications are shown in Table 4. A

Table 4
Experimental engine specifications.

Maximum Power	17 kW at 2200 RPM
Maximum Torque	77.5 N m at 1400 RPM
Bore × Stroke	112 mm × 115 mm
Compression Ratio	16:1
Displacement	1.132 L
Injection Nozzle	7 orifices × 0.115 mm
CRDI Pressure	400–1200 bar
PFI Pressure	2.76 bar
Cooling System	Water

Cummins common rail was connected to a Bosch radial-piston CP3 pump, which was belt driven by a 2 HP DC motor with a pulley ratio of 3:1. The rail was connected to a Bosch piezoelectric injector with a 7×0.115 mm custom nozzle, improving the mechanical injection system [39]. The nozzle was optimized for improved interaction with the omega chamber geometry, modeled based on the OEM injection timing of the engine. The spray angles were reduced ranging from 56° to 68° with reference to injector body axis.

The rail pressure and injection parameters were controlled by a National Instruments (NI) DI driver system, consisting of a NI CompactRIO 9073 controller with a NI 9751 DI Driver (Vieletech) and a NI 9758 PFI driver (Vieletech) in addition to a NI 9215 analog input module and a NI 9411 digital input module. The DI module serves the power required to drive both solenoid and piezoelectric injectors, allowing for control of injection duration and timing for up to six pulses per injector. The timing for injection was determined from crankshaft angles as obtained from an Omron EC63-CW3ZE incremental rotary encoder (accuracy ± 1 rpm, SE 0.007%), which had a resolution of 3600 pulses per revolution. An additional injector is attached to the intake port to inject low reactivity fuels such as n-butanol. This port-fuel injector can be utilized to deliver fuel during intake for fundamental combustion phasing. The experimental setup is shown in Fig. 10.

Data acquisition centered on cylinder pressure in relation to crankshaft positioning for numerous cycles to achieve a proper cycle average from five trial runs (1000 cycles). In-cylinder pressure was measured using a Kistler 6053 cc uncooled piezoelectric pressure transducer (accuracy 0.4%, SE 0.2%) conditioned by a Kistler 5010B dual-mode charge amplifier. The pressure measurement was paired with the crank angle degrees determined with the rotary encoder. Each trial data was acquired from a Yokogawa DL850 Scopetester at a rate of 25 kHz, in conjunction with a LabVIEW DAQ, and AVL Indicom. The Indicom was used for real-time monitoring of combustion phasing based on the crank angle location at which 50% of the fuel mass is burned, CA50. Species such as NO_x, carbon monoxide (CO), aldehydes, and unburned hydrocarbons (UHC) were measured concurrently with an AVL SESAM FTIR V4. Soot concentrations were measured using an AVL 483 Micro Soot sensor (accuracy ± 0.001 mg/m³, SE 3.8%).

Intake flow rate was measured using a Meriam Z50MC-2 laminar flow meter (accuracy $\pm 0.72\%$, SE 0.3%) and LFS-1 computerized system interfaced with atmospheric humidity, temperature and pressure correction. Direct injection fuel consumption was measured using Max Machinery 213 piston flowmeters, where flow was measured from the inlet pump to the CP3 pump and from the return of the fuel injector and the CP3 pump to the fuel tank. A P001 model of the flow meter was used to measure the PFI rate. EGR percentage was determined with the support of

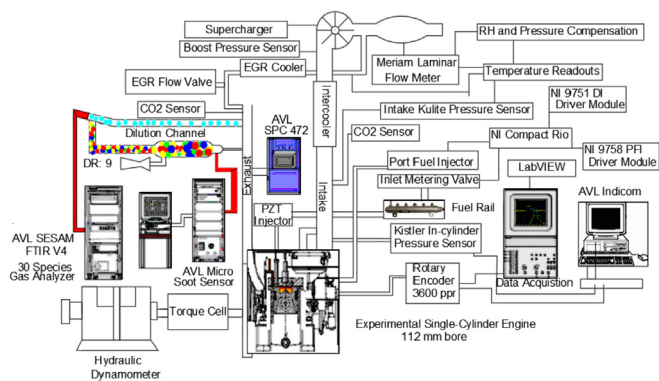


Fig. 10. Experimental engine setup.

EMS 5002 exhaust gas analyzers at the intake and at the exhaust and using the ratio of CO₂ concentration. A butterfly valve at the exhaust was used to increase backpressure for increased EGR flow. A cooler was implemented to reduce temperature of the exhaust gases back to the engine. Exhaust and intake pressure were obtained using Kulite-175-190 M and Omega Px209 pressure transducers at the exhaust before the EGR pipe and intake port, respectively. Boost provided by the supercharger was verified through an additional pressure sensor just after the entrance of the supercharger.

3.1.1. Uncertainty

The full-scale accuracy range of the sensors and the variability of the measurements were used to determine the uncertainty in the measurements for emissions. The uncertainties occur through experimentation as a result of different environmental conditions, different ranges of calibration for instruments, and the experimental method. An approach using root sum of squares method was used to analyze the uncertainty in brake-specific emissions and fuel consumption accounting for the standard error for the criteria needed for calculation. The method used equation (2), where y represents calculated parameters, and x_i represents the measured variables. NO_x, particulate matter, CO, formaldehyde (HCHO), non-methane hydrocarbon (NMHC) emissions, and brake power determination approached uncertainties shown in Table 5.

$$\text{uncertainty}(\%) = 100\% * \sqrt{\sum_{i=1}^n \left[\frac{\partial y}{\partial x_i} \cdot x_i \right]^2} \quad (2)$$

3.2. Experimental operation

The engine data presented showcases methyl oleate in comparison to ULSD#2 during the RCCI mode and conventional diesel combustion (CDC). An investigation of fuel effects on combustion was conducted with a constant combustion phasing with a CA50 by ± 1 CAD compared to the reference. Constant boost of 3 psi and constant intake temperature of 32 °C were maintained. To conduct RCCI, two direct injection pulses were used along with PFI of n-butanol, which was delivered at 340 CAD BTDC after exhaust valve closing. The first direct injection pulse (SOI-1) was set at 60 CAD BTDC for all points while the second injection pulse (SOI-2) was varied to maintain CA50 with each fuel and control ignition delay of the fuel. The operating points across loads are presented in Tables 6–8. For the single injection strategies, as load increased, the main injection was advanced slightly to obtain the target CA50 while SOI-2 for RCCI was delayed closer to TDC.

The second injection pulse had to be advanced for MO RCCI compared to ULSD#2 given the evident difference in cetane number as shown in the CID 510 determination. Rail pressure was increased with load to address rising soot at higher loads. EGR was increased from 20% to 25% as well as PFI from 70% to around 80% to compensate for constant combustion phasing at higher loads. No fuel additives were used during engine operation. ULSD CDC is used to denote ULSD#2 to refer to single injection diesel operation as it is common in literature while MO100 CDC is used to denote the 100% methyl oleate counterpart. The single injection points showcase

Table 5
Measurement uncertainties.

NO _x	Soot	CO	NMHC	HCHO	Brake Power
2.4%	1.7%	2.45%	2.5%	2.33%	2.20%

Table 6
Operating points 4 bar IMEP.

	ULSD RCCI	MO RCCI	ULSD CDC	MO100 CDC
EGR (%)	0	20	20	20
Rail Pressure (bar)	400	400	800	800
SOI-1 mass (%)	65	61.4	—	—
SOI-2 duration (ms)	0.25	0.3	0.788	0.775
SOI-2 timing (CAD)	30	32	17	16
PFI (%)	70	70	—	—

Table 7
Operating points 5 bar IMEP.

	ULSD RCCI	MO RCCI	ULSD CDC	MO100 CDC
EGR (—)	25	25	25	25
Rail Pressure (bar)	400	400	1000	1000
SOI-1 mass (%)	57	52	—	—
SOI-2 duration (ms)	0.3	0.25	0.778	0.78
SOI-2 timing (CAD)	27	32	19	17
PFI (%)	77	79	—	—

Table 8
Operating points 6 bar IMEP.

	ULSD RCCI	MO RCCI	ULSD CDC	MO100 CDC
EGR (—)	25	25	25	25
Rail Pressure (bar)	500	500	1200	1200
SOI-1 mass (%)	61	66	—	—
SOI-2 duration (ms)	0.22	0.16	0.783	0.82
SOI-2 timing (CAD)	5	10	19	18
PFI (%)	77	78	—	—

effects from fuel as well as same operating parameters as RCCI outside injection.

3.3. Combustion characteristics

The in-cylinder pressures for ULSD#2 and MO in RCCI are depicted in Fig. 11. Maximum combustion pressure can be observed to increase up to 43 bars from the motoring pressure. Similar combustion peaks were achieved within 1 bar for both fuels. The differences in cetane number between the fuels were leveled by the injection strategies implemented. Pressure was observed, however, to start rising earlier for MO, given its characteristic high reactivity especially at lower load; the peak additionally shifting by 1 CAD. This trend is more noticeable at in-cylinder pressures for single injection operation as illustrated. Differences between the curves for both operations can be observed; a more abrupt pressure rise inflection can be observed around 350 CAD in the single injection operation compared to smoother rise in pressure observed

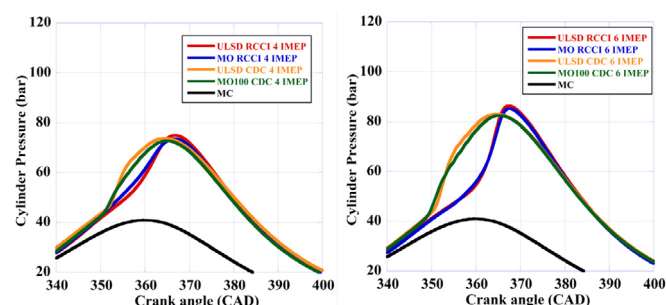


Fig. 11. Cylinder pressure at 4 and 6 bar IMEP.

between 350 and 360 CAD. The peak pressure locations also differ between modes as RCCI had a delayed peak pressure by up to 3 CAD compared to CDC. From the recorded pressures, the apparent heat release rate was determined. Combustion stability improved with higher load across operating modes. CoV of IMEP increased from 2.3% to 1.7% for CDC and RCCI improved from 2.4 to 1.8% as load incremented.

3.4. Apparent heat release rate

The apparent heat release rate (AHRR), shown in Fig. 12, was determined for combustion analysis using equation (2). AHRR was calculated using the calculated swept cylinder volume and linear piston displacement and assuming a closed thermodynamic system throughout combustion, where the in-cylinder contents are assumed to behave as an ideal gas homogeneously [40]. Mass losses due to blow-by or crevice flows were neglected which may account to 2% variation. The configured RCCI strategy allowed for later peak AHRR for MO RCCI compared to ULSD RCCI.

$$\frac{dQ}{d\theta} = \frac{1}{(\gamma - 1)} V \frac{dP}{d\theta} + \frac{\gamma}{(\gamma - 1)} P \frac{dV}{d\theta} \quad (3)$$

Smooth combustion correlated to the shape of the AHRR, which enabled reductions in both NO_x and soot simultaneously compared to CDC. The Gaussian shape of the AHRR resulted in a minimum diffusion stage which is clearly present in single injection operation. A decrease in the diffusion is desired for limiting formation of particulate matter, where radiation from flames at this phase correlate with its production [41]. The higher DCN of methyl oleate led to lower peak AHRR for MO RCCI compared to ULSD RCCI by 5–20%; earlier ignition limited the amount of the premixed phase. The smoother rate can also be inferred to be achieved for MO RCCI as less fuel was utilized in SOI-1 than ULSD RCCI at both 4 and 5 bar IMEP. The peak AHRR was lower at 6 bar IMEP as less fuel was delivered closer to TDC for MO RCCI. The earlier delivery of FAME during RCCI also resulted in a less readily-combustive outcome in relation to diesel.

The single fuel injection operations showed a clear lower peak AHRR for MO100 CDC compared to ULSD CDC. The maximum heat release rates were lower at 5 and 6 bar IMEP for the single injection operations. Higher reactivity of the neat methyl oleate lead earlier ignition and less premixed phase. This consequently increased the magnitude of the diffusion phase in comparison to ULSD CDC; the length of the diffusion was, however, slightly shorter for the methyl oleate. The maximum heat release rate phased forward for the RCCI operations as load increased while the maximum AHRR for ULSD CDC and MO100 CDC lagged. This correlates with the magnitude of diffusion for the single injection operations, which affected the combustion phasing in accordance to CA50. ULSD CDC was delivered at an earlier injection timing and shorter injection duration

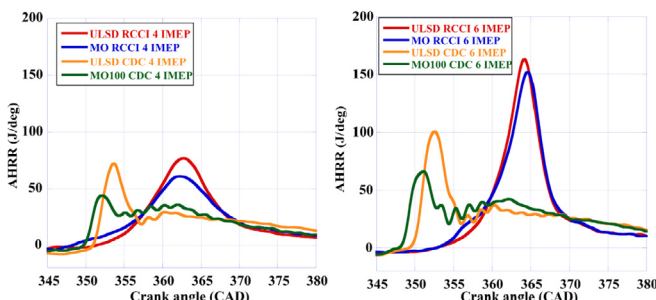


Fig. 12. Apparent heat release rate at 4 and 6 bar IMEP

compared to MO100 CDC. The movement of peak AHRR is clear with the selected SOI as location for maximum premixing is similar for both 5 and 6 bar IMEP. Moreover, it is significant to notice the ratio of premixed to diffusion heat release increased at higher load. The ratio was higher for ULSD CDC, related to the higher equivalence ratio of diesel compared to MO100 CDC.

3.5. Instantaneous volume-averaged gas temperatures

Instantaneous in-cylinder combustion temperatures were determined using the corrected in-cylinder pressures and volume of the cylinder, varying with piston movement and modeled based on the ideal gas law and assuming homogenous gas contents. The ideal gas law was followed as the mean kinetic energy of the molecules of the air-fuel mixture can be assumed as proportional to the overall bulk temperature. Wall temperatures do not follow the combustion gas temperature because the time is not sufficient for heat from combustion to be absorbed by the walls before the exhaust valve opens. The volumetric efficiency was found to be the same for all loads at constant speed at constant ambient air temperatures and pressures into the intake. The in-cylinder combustion temperatures for 6 bar IMEP are shown in Fig. 13, which fit in the realm of low temperature combustion [42].

The single-injection runs had both an earlier temperature rise as well as later temperature decrease compared to RCCI, increasing time in high temperature region. A slightly higher temperature can also be perceived for the single fuel runs due to the lack of n-butanol; the alcohol absorbed heat of vaporization at a much higher rate than the high reactivity fuels, creating a cooling effect during compression. The increase in PFI ratio as load increased also delayed the temperature rise, leading to differing thermal gradients. At 4 bar IMEP, ULSD RCCI showed a delayed temperature rise in the cylinder as the load was more sensitive to higher reactivity methyl oleate injected at SOI-2. The temperature decreased faster than MO RCCI at this load, correlating to absence of EGR. ULSD RCCI also achieved a higher temperature at 5 bar IMEP, as more pre-mixing occurred compared to other loads due to the selected injection timings. This compounds with the higher SOI-1 fraction and delayed SOI-2 location compared to MO RCCI allowing for more

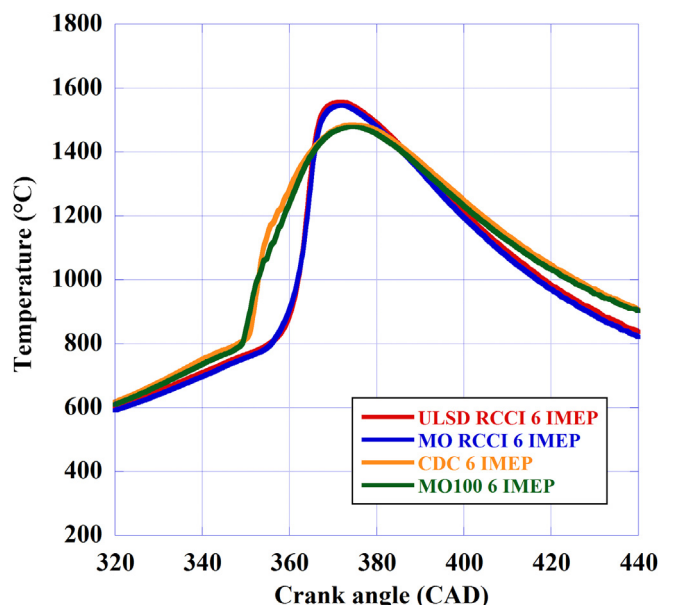


Fig. 13. In-cylinder gas temperatures at 6 bar IMEP.

interaction of the spray with the induced charge.

At 6 bar IMEP, the temperature profile was equivalent for both load operations as the mixture was less prone to change with the physical properties of the FAME compared to diesel; the maximum AHRR for both RCCI modes were similar, albeit with different peak locations. The temperature rise was more prolonged for MO100 CDC at the lower loads, due to smoother combustion, compared to ULSD CDC. Peak AHRR was steadily higher than MO100 CDC due to its reactivity and later injection timing. Higher oxygen content additionally promoted leaner operation, limiting rapid burning of the FAME. The steadier buildup in temperature is desired to obtain less NO_x emissions, as the residence time in the high temperature combustion was shortened. Formation of NO_x still occurs due to thermal effects, yet, does represent the whole bulk of its production due to low operating in-cylinder temperatures. Prompt NO_x would be favored by such temperature levels in local rich areas in the cylinder.

3.6. Ringing Intensity

Ringing intensity (RI), illustrated in Fig. 14, was calculated given its correlation with overall combustion noise. RI was determined using equation (3), which considers the maximum pressure, PPRR, and peak temperature. A standard value of 0.05 was used for β , which relates pulsation amplitude to the pressure derivative and has been used for engines of varying displacements [43]. Cooled EGR and lower intake temperatures were used to prevent knocking effects from high premixing at the tested loads as seen also in the literature [44]. RI decreased for RCCI compared to the single injection operation at 4 and 5 bar IMEP, as expected from the stratified fuel delivery. CDC points were delivered at a high rail pressure which prevented higher peak premixing, yet, peak AHRR was more prolonged and occurred before TDC in compression.

$$RI = \frac{1}{2\gamma} \frac{\beta \left(\frac{\delta P}{\delta t_{max}} \right)}{P_{max}} \sqrt{\gamma R T_{max}} \quad (4)$$

At 6 bar IMEP, ULSD RCCI achieved the highest RI due to its high heat release rate as well as injection closer to TDC, representing a less stratified fuel delivery. Injections closer to the cylinder can be assumed to lead to this effect as fuel is delivered into a higher

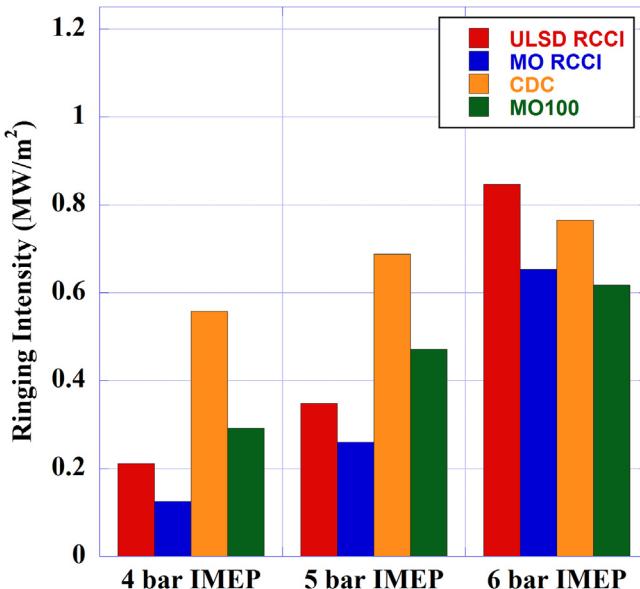


Fig. 14. Ringing Intensity across loads.

temperature zone. MO had a lower RI than CDC, correlating to smoother temperature rise and limited premixing. Peak pressures were also closer to TDC for single injections, compounding on the increase in RI in relation to RCCI mode. MO RCCI had the lowest RI at 4 and 5 bar IMEP correlating with the stratified delivery of the fuel and the molecular composition of the methyl ester. At 6 bar IMEP, MO RCCI is higher than MO100 CDC, relating to higher peak AHRR exhibited by RCCI as well as detected maximum temperatures. Additional EGR will be needed for RCCI at 6 bar IMEP to allow for advanced SOI-2 as encountered in 4 and 5 bar IMEP. The EGR will minimize the number of reactive components in the intake charge; a richer mixture can lead to elevated rates of pressure rise when fuel is delivered before combustion at TDC.

3.7. Mass fraction burned

The mass burned, shown in Fig. 15, was calculated from the integral of the net heat release rate for analysis of ignition delay, combustion duration, and combustion phasing. The main parameters used were CA10, CA50, and CA90 (10%, 50%, and 90% fuel mass fraction burned, respectively). The ignition delay (ID) was defined as the duration from the main injection to the start of combustion (CA10), which is a common definition used previously for low temperature combustion [45]. The ID was significantly different for both combustion modes, where the difference in CA10 between modes was higher as load increased, reaching up to 9 CAD. The combustion duration was measured as the period from CA10 to CA90. The end of combustion is not taken as later than CA90 as the remaining fraction does not completely burn and can be lost to crevices and exhaust valve. The combustion duration increased with higher load for single injection operation; this trend was reversed for RCCI modes as a result of combustion efficiency increasing from rising temperatures, allowing more efficient burn in a limited time frame. The operation of MO RCCI offered more reactivity through direct injection, which decreased the amount of fuel delivered of SOI-1. This change in injection mass effectively changes the local concentrations before high temperature combustion in the cylinder. This behavior can be perceived in the burn rate across all the tested loads.

At 4 bar IMEP, the single injection operations show the highest difference in the burn curve, as the combustion efficiency was much lower for ULSD CDC than MO100 CDC. This can be related to the injection timing and rail pressure used to operate the points. MO100 CDC, however, starts burning before ULSD CDC, correlating with its higher DCN. This can also be perceived in RCCI, where MO ignites faster than ULSD in the cycle. The burn rate for MO100 CDC decreases around CA50, as a result of the air utilization before peak compression. At the same load, ULSD#2 shows a delayed ignition even with the absence of EGR, which characteristically enabled similar burn rate across the midpoint of combustion.

At 5 bar IMEP, a higher fraction of MO RCCI was delivered at an

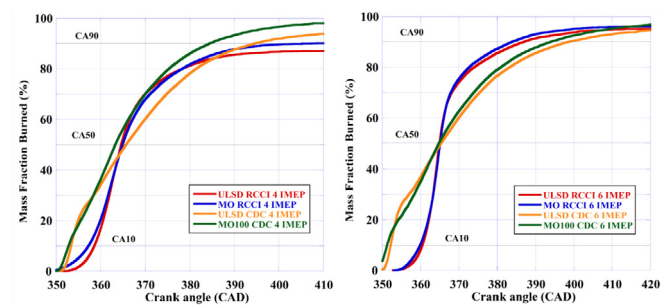


Fig. 15. Mass fraction burned at 4 and 6 bar IMEP

advanced timing compared to ULSD RCCI, limiting the mixing and slowing down the burn rate at similar EGR rate. This was done to achieve a 20% longer ignition delay for MO RCCI compared to ULSD RCCI, thereby controlling CA50. At 6 bar IMEP, the burn curves do not seem affected directly by the delayed SOI-2 in RCCI; the burn rate did notably increase as load progressed due to higher implemented premixed fuel ratios. Ignition was faster, however, for ULSD RCCI compared to MO RCCI due to the more fuel being injected closer to TDC, necessary to maintain CA50. The introduction of high reactivity fuel closer to TDC could, however, lead to higher formation of thermal NOx as temperatures are found the highest during the cycle. The single injection operations also had similar overall burning resulting from the selected strategy due to the richer combustion.

3.8. Heat losses

Heat transfer was analyzed due to its contribution in the loss of fuel efficiency in the engine cycle. It occurs through recognizable thermal boundaries through which gases change in temperature and the largest gradient occurs at the cylinder wall. The heat losses were analyzed through heat fluxes, which were determined by using a model based on paper from Borman and Nishiwaki [46] and revised by Soloiu et al. [47] using the modeled in-cylinder temperatures (T_A). The model, as detailed in equation (4), implemented semi-empirical constants, a uniform cylinder wall temperature (T_W), in-cylinder Reynolds number (Re), and air thermal conductivity (λ_A).

$$\dot{q}(\alpha) = A \frac{\lambda_A(\alpha)}{D} Re^{0.7} (T_A(\alpha) - T_W) + \sigma^* e (T_A^4(\alpha) - T_W^4) \quad (5)$$

Convection heat flux mapping was simulated using a revised model from Annand and Ma [48] in place to obtain λ_A . The convective heat transfer is related to the heat contact established by combustion gases with the cylinder walls, piston crown, and cylinder head. The bulk of combustion heat transfer is taken by convection; flame and spray interaction dominated heat movement within the cylinder. This trend is further expected in LTC as modern strategies lean toward decreasing the diffusion phase for soot control. The radiative heat transfer was thus simulated assuming black body radiation from the soot particles, which correlates with the heat generated from diffusion flames using the Stefan-Boltzmann constant (σ). The radiation flux followed the maximum temperature crank angle degree. The Reynolds number was determined using equation (6) for characterizing the flow regimes in the cylinder. Droplet breakup is promoted by high turbulence around compression indicated by a high Re. The Re determination used the in-cylinder gas density (ρ_A) and viscosity (μ_A) at every 0.18 CAD while estimating turbulence correspondingly to experimental engine speed (N), stroke (S), and bore (D). Convection flux followed the phasing shown with the calculated Re curve across the engine cycle. Differences in convection and radiation were more evident at higher load, which can be attributed to higher relative air-fuel ratio at the lower load. The losses were determined to show a ratio of radiation to convection heat losses close to 0.2. For CDC, losses occurred before TDC due to sudden combustion close to the operated injection timing.

$$Re(\alpha) = \rho(\alpha) \frac{S \cdot N \cdot D}{30\mu(\alpha)} \quad (6)$$

RCCI reduced the area for heat transfer while increasing the peak magnitude. This trend allowed for lower emissions formation due to encompassed combustion duration by the single injection strategies. The fluxes lagged compared to the presented

instantaneous temperature which relates to the travel of heat in the cylinder. When integrating the heat fluxes into the heat release though calculation of the piston area, the total fuel energy lost in heat transfer can be plotted. The gross heat release curves for 6 bar IMEP operating points are provided in Fig. 16. The gross heat release is presented considering losses due to convection, radiation, crevice effects, and fuel vaporization. Relative magnitude to the net heat release rate can then be identified; 70 ± 3% of the fuel energy is accounted for the net heat release. The heat losses can be observed to begin earlier in the cycle for the single injection operations. Radiation encompassed 5% of the radiation losses for all points. Convection comprised roughly 18% for RCCI and 21% for single injection points. Convection comprised roughly 18% for RCCI and 21% for single injection points.

4. Emissions and efficiencies

NO_x values decreased with the load for MO RCCI correlating to lower peak release rate. At 6 bar IMEP, an 80% decrease in NO_x was achieved for MO RCCI compared to ULSD RCCI. Soot emissions were continuously lower for MO than ULSD given the molecular oxygen present in double bond within the methyl ester. A 70–80% decrease was observed for soot in RCCI and 20–30% decrease in CDC. Compared to single injection, NO_x and soot simultaneously dropped by several orders with RCCI at the same boost, EGR rate, intake temperature, and CA50 at each corresponding load which can be seen in a logarithmic scale in Figs. 17 and 18. The NO_x emissions did not follow a tendency with peak combustion temperatures but rather with the residence time of high temperature combustion, which was extended for CDC compared to RCCI as seen in the combustion analysis. NO_x decreased linearly as rail pressure was increased by 200 bars for meeting CA50 with the same EGR rates. MO100 CDC increased NO_x production compared to ULSD CDC, which was promoted by the oxygen concentration of the FAME.

Stratifying the fuel delivered as well as varying the reactivity in the cylinder achieved a variable local equivalence ratio. This resulted in an overall lower soot formation given extended ignition delay, therein allowing proper mixing and minimal to no diffusion. The oxygen content of n-butanol also remitted the soot precursors. Soot in RCCI exhibited a downward trend with load as more PFI was necessary to delay combustion phasing. NO_x in RCCI increased as a tradeoff due to more available oxygen for prompt NO_x and higher overall premixing. For single injection operations, heat transfer was substantially different in its duration, allowing for higher diffusion rivaling the premixed phase combustion magnitude.

The lower combustion temperatures resulting from RCCI did affect combustion efficiency at the lower loads. RCCI strategies at 6 bar IMEP achieved lower CO and equivalent or lower NMHC emissions compared to ULSD CDC as observed in Fig. 19. CO and NMHC were both lower across loads for methyl oleate during RCCI and single fuel injection operation compared to ULSD counterparts.

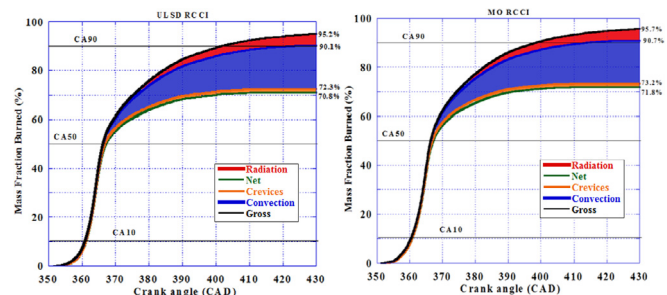


Fig. 16. Gross heat release composition of ULSD RCCI and MO RCCI at 6 bar IMEP.

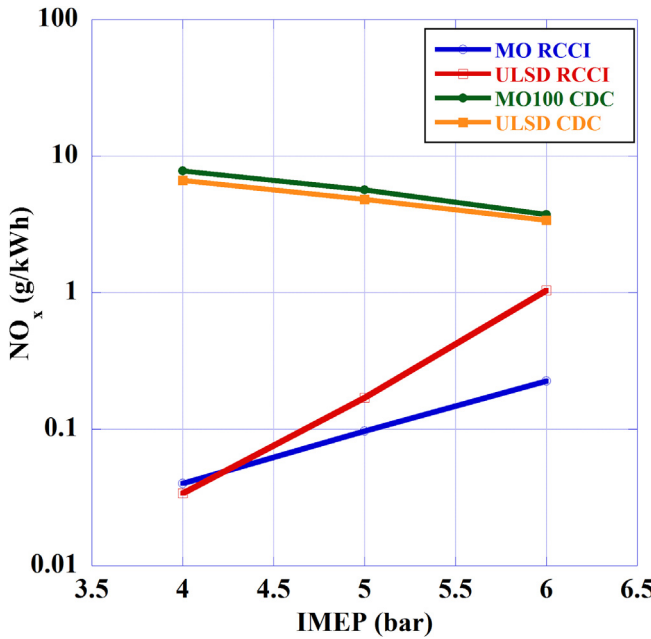
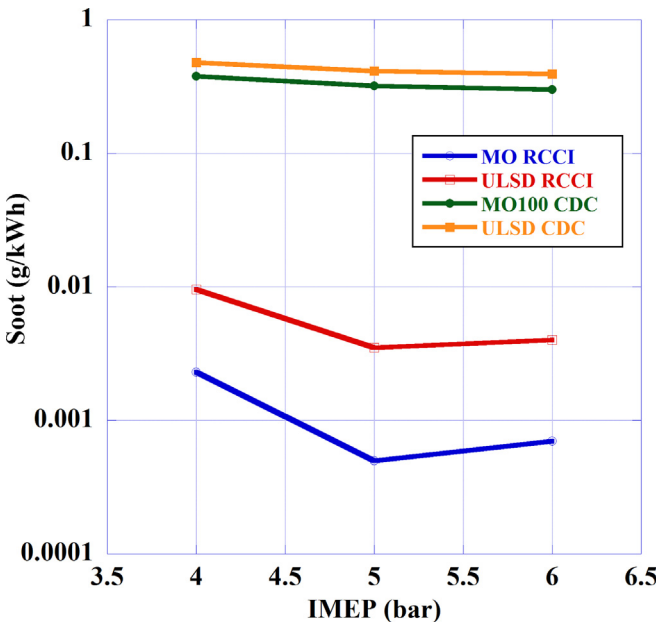
Fig. 17. Brake specific NO_x emissions at 1500 RPM.

Fig. 18. Brake specific soot emissions at 1500 RPM.

This can be related to a leaner operation as well more effective burn of the FAME at same boost. A higher flash point could have additionally allowed for further penetration into cylinder, allowing for air-fuel mixing. Although highly reactive, the FAME had a lower vaporization rate which benefited a more complete combustion due to more residence time for premixing with surrounding in-cylinder air. MO RCCI at 6 bar IMEP met EPA Tier 4 standards for off-road engines.

The high magnitude of the CO levels can be related to the lean operation at lower loads for RCCI coupled with the low temperature combustion. The increase in CO for ULSD CDC and MO100 CDC can be related to more advanced injection timings used for combustion phasing, which led to higher possibilities for fuel impingement to cylinder walls. This effectively supports the use of multipulsed injections for stratified fuel delivery and prevent overlong

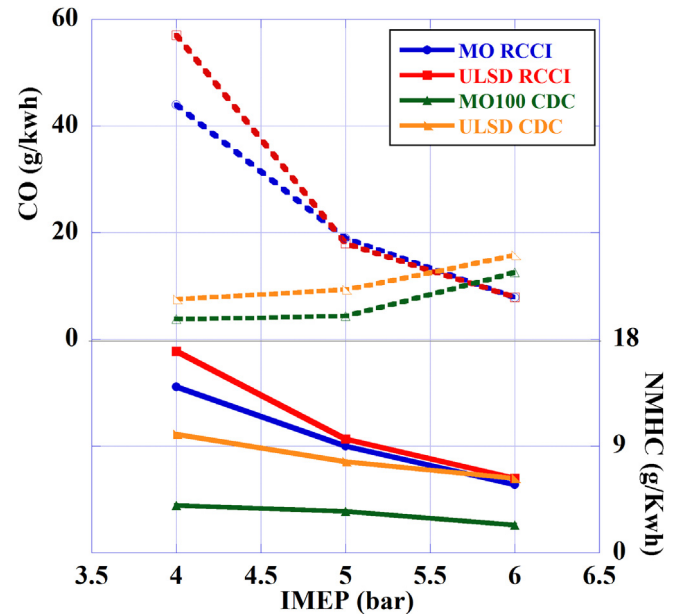


Fig. 19. Brake specific CO and NMHC emissions at 1500 RPM.

combustion. The global relative air-fuel ratio (λ) for each operating point is provided in Table 9. The stoichiometric air-fuel ratio was calculated for each neat fuel through oxidation reaction in which ULSD, methyl oleate, and n-butanol had ratios of 14.6, 11.5, and 12.6, respectively. The air-fuel ratio decreased with load because of constant boost operation. The highest λ was for ULSD RCCI at 4 bar IMEP given there was no use of EGR. MO RCCI had a lower air-fuel ratio, correlating to increased fuel usage.

Formaldehyde emissions are presented in Fig. 20, as these emissions although unregulated have shown increased formation with the use of alcohol in combustion [49]. These aldehydes were increased for ULSD RCCI and MO RCCI compared to the CDC operations; the other aldehydes were considered negligible. The magnitude of the increase in aldehydes decreased as load increased. This can be related to higher combustion efficiency and the presence of molecular oxygen in the cylinder. This assumption can be supported by the higher aldehydes occurring during MO100 CDC operation.

Energy specific fuel consumption (ESFC), detailed in Fig. 21, was determined for the operations, showing overall energy consumption needed by the combustion cycle. It was calculated from the sum of the fuel mass flow rates times the characteristic LHV divided by the effective power (P_{eff}) as shown in equation (7). This analyzed the energy provided overall by the fuel to the cycle due to the presence of two fuels. The ESFC decreased with load, correlating with the fuel consumption curve for the engine.

$$\text{ESFC} = \frac{\sum_{i=1}^2 LHV_i * \dot{m}_{\text{fuel}}}{P_{\text{eff}}} \quad (7)$$

The lower energy content of n-butanol led to higher ESFC for RCCI at 4 bar IMEP. At this load, MO RCCI was the highest due to

Table 9
Relative air-fuel ratio (λ) at 1500 RPM.

	4 bar IMEP	5 bar IMEP	6 bar IMEP
ULSD RCCI	4.50	3.91	3.34
MO RCCI	3.72	3.36	3.01
ULSD CDC	4.23	3.64	3.27
MO100 CDC	4.34	4.01	3.3

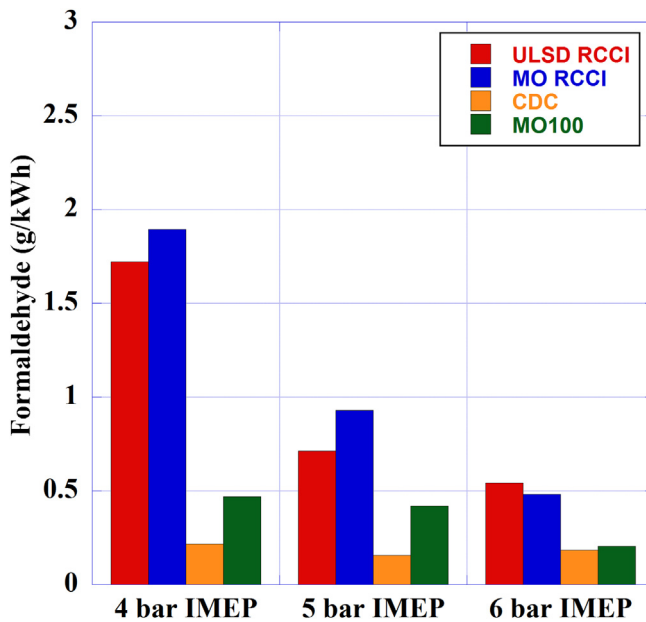


Fig. 20. Brake specific formaldehyde emissions at 1500 RPM.

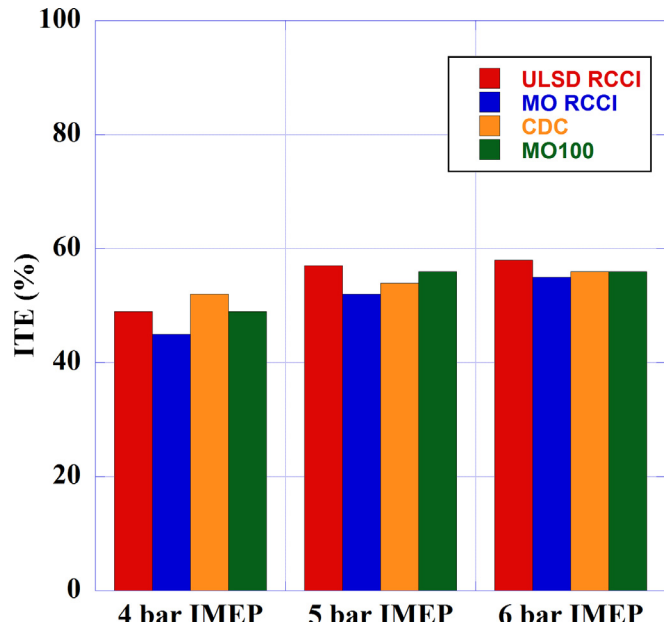


Fig. 22. Indicated thermal efficiencies across loads.

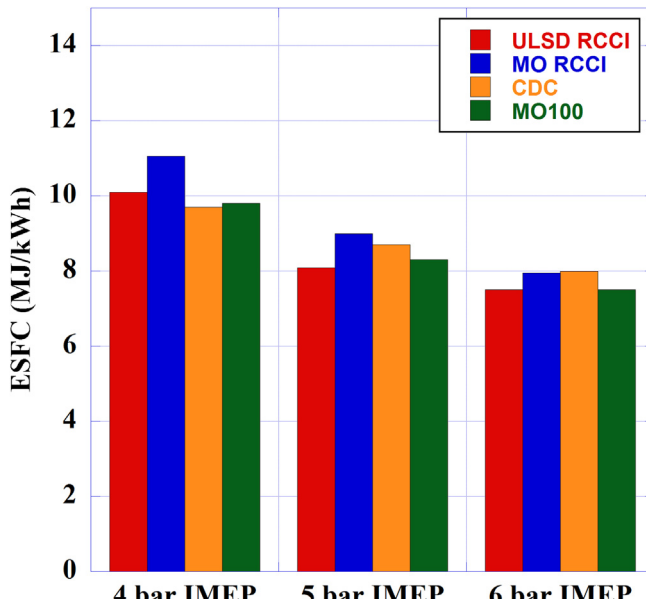


Fig. 21. Energy specific fuel consumption at 1500 RPM.

combined lower energy content of both FAME and alcohol. This holds overall at the following loads although at a lower difference from the single fuel operation. Higher ESFC for ULSD CDC at 6 bar IMEP can be attributed to increase in CO emissions and the difference in heat transfer compared to RCCI. Higher lubricity from MO100 CDC could also allow for lower friction losses overall at 6 bar IMEP even though the FAME possessed lower energy content compared to ULSD. Additionally, lower heat transfer losses can be attributed to improve the efficiency of the implemented FAME.

Gross indicated thermal efficiencies (ITE), not accounting for losses from the supercharger and the electronic actuated injection system, are detailed in Fig. 22. ITE was equivalent for both ULSD and MO100 in CDC at 6 bar IMEP even with increased combustion efficiency for methyl oleate due to the reduced heat transfer to the walls

at the load point and lower heating value of FAME. The higher conversion rate of the molecular composition of the FAME can be attributed to its oxygen content as burn rate as observed in the TGA also. ULSD RCCI had higher ITE as more fuel was burned closer to the TDC as a result of the reactivity stratification. MO RCCI as the ITE for ULSD was consistently higher in dual fuel combustion due to the higher energy density; in contrast, MO100 had a higher ITE at 5 bar IMEP correlating with the burn rate at the lower equivalence ratio. The constant combustion phasing utilized indicated fuel behavior was particularly dependent on the set kinetics at lower loads. Mechanical efficiencies improved from 75% to 83% as load increased. Higher mechanical efficiency for MO100 CDC was observed due to decreased friction achieved by higher lubricity of the FAME compared to the diesel. Overall, the mechanical efficiencies were maintained within 2% at each operating load, where RCCI maintained similar efficiencies and reduced emissions by minimizing heat losses in-cylinder.

5. Conclusion

RCCI operation with methyl oleate was investigated along n-butanol PFI in order to identify the potential use of a single FAME as a surrogate for biodiesel in dual fuel operation as well as the concept of using two sustainable fuels in dual fuel combustion. The oxygen content of the FAME and the alcohol was also a factor in increasing the molecular oxygen present in the cylinder. MO performance was compared with a with ULSD#2 reference at the same engine speed and loads under constant combustion phasing. For effective MO operation, SOI-2 timing had to be advanced and its fraction increased to allow for utilization of the higher reactivity FAME at same CA50, increasing ignition delay by 10–15% compared to ULSD RCCI. Methyl oleate operation in RCCI allowed similar peak cylinder pressures within 1 bar and lower maximum heat release rates by 5–20% compared to ULSD. CoV of IMEP in RCCI was maintained similar to CDC under 2.5%.

The dual DI strategy selected for RCCI additionally allowed an AHRR with low pressure gradients from fuel stratification. RI consequently decreased by up to 70% with RCCI compared to CDC as a result of the smooth combustion. Minimum diffusion was

encountered with RCCI, limiting the radiative heat transfer after TDC. Reactivity stratification of the FAME as well as lower overall combustion temperatures and higher oxygen content allowed both lower NO_x and soot than ULSD#2 at 5 and 6 bar IMEP. NO_x and soot decreased a maximum of 80% across operating points for MO RCCI compared to ULSD RCCI. CO and NMHC increased at 4 and 5 bar IMEP for RCCI compared to CDC, resulting from lean combustion and low temperatures. Combustion efficiency improved, however, for methyl oleate in both RCCI and CDC compared to ULSD, relating to its unsaturated components facilitating oxidation. Methyl oleate was observed to allow better in-cylinder emissions control overall with selected strategies and loads at similar engine mechanical efficiencies as encountered with ULSD CDC.

5.1. Future work

Authors believe that future research should use higher boost at loads over 5 bar IMEP to obtain the desired lean mixture and be able to inject at timings equivalent to those at the lower loads in this study. This should also allow the injection of high PFI rates at the higher loads and would not decrease the overall relative air-fuel ratio. Noise, vibrations, and harshness should be investigated to ascertain the effects of methyl oleate combustion on the mechanical components in both RCCI and single fuel operation. Benefits from lower ringing intensities could be correlated with sound pressure measurements at the investigated loads.

Acknowledgments

We thank the National Science Foundation for support through Grant No. 1609524. Gratitude to Charles McGuffey from PAC, Timothy Martin from MKS Instruments, Daniel Stockton from AVL, Matt Viele from Vieletech, Samuel Olesky from Kistler and Sophia Fleri from GSU for their support..

List of Abbreviations

AHRR	Apparent Heat Release Rate
BSFC	Brake Specific Fuel Consumption
BTDC	Before Top Dead Center
CA10	Crank angle at which 10% fuel mass burned
CA50	Crank angle at which 50% fuel mass burned
CA90	Crank angle at which 90% fuel mass burned
CAD	Crank Angle Degree
CD	Combustion Delay
CDC	Conventional Diesel Combustion
CO	Carbon Monoxide
CO ₂	Carbon Dioxide
CoV	Coefficient of Variation
cP	centiPoise
DAQ	Data Acquisition
DI	Direct Injection
DTA	Differential-thermo Analysis
EGR	Exhaust Gas Recirculation
EPA	Environmental Protection Agency
ESFC	Energy Specific Fuel Consumption
FTIR	Fourier Transformed Infrared
HCCI	Homogenous Charge Compression Ignition
IMEP	Indicated Mean Effective Pressure
ITE	Indicated Thermal Efficiency
LHV	Lower Heating Value
MC	Motoring Curve
MO	Methyl Oleate
MO100	100% Methyl oleate direct injection
NI	National Instruments

NMHC	Non-methane hydrocarbons
NO _x	Nitrogen Oxide
PCCI	Premixed Charge Compression Ignition
PFI	Port Fuel Injection
PPCI	Partially Premixed Compression Ignition
PPRR	Peak Pressure Rise Rate
PM	Particulate Matter
RCCI	Reactivity Controlled Compression Ignition
RI	Ringing Intensity
SE	Standard Error
SMD	Sauter Mean Diameter
SOI	Start of Injection
SOI-1	First direct injection in RCCI
SOI-2	Second direct injection RCCI
TDC	Top Dead Center
TGA	Thermo-gravimetric Analysis
ULSD	Ultra-Low Sulfur Diesel
γ	Ratio of specific heats

References

- [1] Stanglmaier RH, Roberts CE. Homogeneous charge compression ignition (HCCI): benefits, compromises, and future engine applications. SAE International; 1999. SAE Technical Paper 1999-01-3682.
- [2] Benajes J, Molina S, García A, Monsalve-Serrano J. Effects of direct injection timing and blending ratio on RCCI combustion with different low reactivity fuels. Energy Convers Manag 2015;99:193–209.
- [3] Laguitton O, Crua C, Cowell T, Heikal MR, Gold MR. The effect of compression ratio on exhaust emissions from a PCCI diesel engine. Energy Convers Manag 2007;48(11):2918–24.
- [4] Nieman DE, Dempsey AB, Reitz RD. Heavy-duty RCCI operation using natural gas and diesel. SAE Int J Eng 2012:270–85.
- [5] Inagaki K, Fuyuto T, Nishikawa K, Nakakita K, Sakata I. Dual-fuel PCI combustion controlled by in-cylinder stratification of ignitability. SAE International; 2006. SAE Technical Paper 2006-01-0028.
- [6] Reitz RD, Duraisamy G. Review of high efficiency and clean reactivity controlled compression ignition (RCCI) combustion in internal combustion engines. Prog Energy Combust Sci 2015;46:12–71.
- [7] British Petroleum Company. BP statistical review of world energy, london. 2017.
- [8] Kokjohn SL, Hanson RM, Splitter DA, Reitz RD. Fuel reactivity controlled compression ignition (RCCI): a pathway to controlled high-efficiency clean combustion. Int J Engine Res 2011;12(3):209–26.
- [9] DelVescovo D, Kokjohn S, Reitz R. The effects of charge preparation, fuel stratification, and premixed fuel chemistry on reactivity controlled compression ignition (RCCI) combustion. SAE Int J Eng 2017;10(4).
- [10] Pohlkamp K, Reitz RD. Reactivity controlled compression ignition (RCCI) in a single-cylinder air-cooled HSDI diesel engine. SAE International; 2012. SAE Technical Paper 2012-32-0074.
- [11] Splitter D, Hanson R, Kokjohn S, Reitz RD. Reactivity controlled compression ignition (RCCI) heavy-duty engine operation at mid-and high-loads with conventional and alternative fuels. SAE International; 2011. SAE Technical Paper 2011-01-0363.
- [12] Curran S, Hanson R, Wagner R. Effect of E85 on RCCI performance and emissions on a multi-cylinder light-duty diesel engine. SAE International; 2012. SAE Technical Paper 2012-01-0376.
- [13] Zou X, Wang H, Zheng Z, Reitz R, Yao M. Numerical study of the RCCI combustion processes fuelled with methanol, ethanol, n-butanol and diesel. SAE International; 2016. SAE Technical Paper 2016-01-0777.
- [14] Han X, Yang Z, Wang M, Tjong J, Zheng M. Clean combustion of n-butanol as a next generation biofuel for diesel engines. Appl Energy 2017;198:347–59.
- [15] Valentino G, Corcione FE, Iannuzzi SE, Serra S. Experimental study on performance and emissions of a high speed diesel engine fuelled with n-butanol diesel blends under premixed low temperature combustion. Fuel 2012;92(1): 295–307.
- [16] Leermakers CAJ, Bakker PC, Somers LMT, de Goey LPH, Johansson BH. Butanol-diesel blends for partially premixed combustion. SAE Int J Eng 2013;6(1).
- [17] Soloiu V, Duggan M, Harp S, Vlcek B, Williams D. PFI (port fuel injection) of n-butanol and direct injection of biodiesel to attain LTC (low-temperature combustion) for low-emissions idling in a compression engine. Energy 2013;52:143–54.
- [18] Environmental Protection Agency. Renewable fuel standard program: standards for 2018 and biomass-based diesel volume for 2019, 40 C.F.R. § 80.1405. 2017.
- [19] Mofijur M, Atabani AE, Masjuki HH, Kalam MA, Masum BM. A study on the effects of promising edible and non-edible biodiesel feedstocks on engine performance and emissions production: a comparative evaluation. Renew Sustain Energy Rev 2013;23:391–404.

- [20] Karra PK, Veltman MK, Kong S-C. Characteristics of engine emissions using biodiesel blends in low-temperature combustion regimes. *Energy Fuel* 2008;22(6):3763–70.
- [21] Zhao F, Yang W, Yu W, Li H, Sim YY, Liu T, Tay KL. Numerical study of soot particles from low temperature combustion of engine fueled with diesel fuel and unsaturation biodiesel fuels. *Appl Energy* 2018;211:187–93.
- [22] Mofijur M, Rasul MG, Hyde J, Azad AK, Mamut R, Bhuiya MMK. Role of biofuel and their binary (diesel–biodiesel) and ternary (ethanol–biodiesel–diesel) blends on internal combustion engines emission reduction. *Renew Sustain Energy Rev* 2016;53:265–78.
- [23] Ramey D, Yang S-T. Production of butyric acid and butanol from biomass. U.S. Department of Energy; 2004.
- [24] Jin C, Yao M, Liu H, Lee C-fF, Ji J. Progress in the production and application of n-butanol as a biofuel. *Renew Sustain Energy Rev* 2011;15(8):4080–106.
- [25] Knothe G, Matheaus AC, Ryan TW. Cetane numbers of branched and straight-chain fatty esters determined in an ignition quality tester☆. *Fuel* 2003;82(8):971–5.
- [26] J. E, Liu T, Yang WM, Li J, Gong J, Deng Y. Effects of fatty acid methyl esters proportion on combustion and emission characteristics of a biodiesel fueled diesel engine. *Energy Convers Manag* 2016;117:410–9.
- [27] Altaie MAH, Janius RB, Rashid U, Taufiq-Yap YH, Yunus R, Zakaria R, Adam NM. Performance and exhaust emission characteristics of direct-injection diesel engine fueled with enriched biodiesel. *Energy Convers Manag* 2015;106:365–72.
- [28] Sukjit E, Herreros JM, Dearn KD, García-Contreras R, Tsolakis A. The effect of the addition of individual methyl esters on the combustion and emissions of ethanol and butanol -diesel blends. *Energy* 2012;42(1):364–74.
- [29] Soloiu V, Weaver J, Ochieng H, Duggan M, Davoud S, Vlcek B, Jenkins C, Butts C. Experimental study of combustion and emissions characteristics of methyl oleate, as a surrogate for biodiesel, in a direct injection diesel engine. In: SAE 2013 world congress, SAE international, SAE technical paper 2013-01-1142, Detroit, MI; 2013.
- [30] Soloiu V, Lewis J, Covington A, Nelson D, Schmidt N. Oleic methyl ester investigations in an indirect injection diesel engine; stage one: combustion investigations. *SAE Int. J. Fuels Lubr.* 2011;4(1):58–75.
- [31] Hanson RM, Reitz RD. Effects of biofuel blends on transient reactivity-controlled compression ignition engine combustion. *Int J Engine Res* 2016;17(8):857–65.
- [32] Soloiu V, Simons E, Muinos M, Harp S, Knowles A, Molina G. Sound and vibration levels of CI engine with synthetic kerosene and n-butanol in RCCI. *SAE International*; 2016. SAE Technical Paper 2016-01-1306.
- [33] Kinney AJ, Clemente TE. Modifying soybean oil for enhanced performance in biodiesel blends. *Fuel Process Technol* 2005;86(10):1137–47.
- [34] Soloiu V, Gaubert R, Moncada J, Harp S, Flowers K, Ilie M. Partially premixed compression ignition of fischer tropesch synthetic paraffinic kerosene (S8) with PFI of n-butanol. In: ASME 2017 internal combustion engine fall technical conference, ASME ICEF2017-3674, Seattle, WA; 2017. p. 14.
- [35] Wadumestrige K, Ng KYS, Salley SO. Properties of butanol-biodiesel-ULSD ternary mixtures. *SAE Int. J. Fuels Lubr.* 2010;3(2):660–70.
- [36] Lapuerta M, Sanz-Argent J, Raine R. Heat release determination in a constant volume combustion chamber from the instantaneous cylinder pressure. *Appl Therm Eng* 2014;63(2):520–7.
- [37] ASTM D7668-14a. Standard test method for determination of derived cetane number (DCN) of diesel fuel oils—ignition delay and combustion delay using a constant volume combustion chamber method. West Conshohocken, PA: ASTM International; 2014.
- [38] Lebedeva S, Lebedeva G, Sendzikiene E, Makareviciene V. Investigation of the performance and emission characteristics of biodiesel fuel containing butanol under the conditions of diesel engine operation. *Energy Fuel* 2010;24(4):4503–9.
- [39] Soloiu V, Moncada JD, Gaubert R, Muñoz M, Harp S, Ilie M, Zdanowicz A, Molina G. LTC (low-temperature combustion) analysis of PCCI (premixed charge compression ignition) with n-butanol and cotton seed biodiesel versus combustion and emissions characteristics of their binary mixtures. *Renew Energy* 2018;123:323–33.
- [40] Heywood J. Internal combustion engine fundamentals. New York, NY: McGraw-Hill Companies; 1988.
- [41] Benajes J, Martín J, García A, Villalta D, Warey A. In-cylinder soot radiation heat transfer in direct-injection diesel engines. *Energy Convers Manag* 2015;106:414–27.
- [42] Neely GD, Sasaki S, Huang Y, Leet JA, Stewart DW. New diesel emission control strategy to meet US tier 2 emissions regulations. SAE International; 2005. SAE Technical Paper 2005-01-1091.
- [43] Eng JA. Characterization of pressure waves in HCCI combustion. In: SAE Powertrain & Fluid Systems Conference and Exhibition, SAE International, San Diego, CA; 2002.
- [44] Dec JE, Yang Y. Boosted HCCI for high power without engine knock and with ultra-low NO_x emissions – using conventional gasoline. *SAE Int J Eng* 2010;3(1):750–67.
- [45] Joshi U, Zheng Z, Shrestha A, Henein N, Sattler E. An investigation on sensitivity of ignition delay and activation energy in diesel combustion. *J Eng Gas Turbines Power* 2015;137(9). 091506-091506-8.
- [46] Borman G, Nishiwaki K. Internal-combustion engine heat transfer. *Prog Energy Combust Sci* 1987;13(1):1–46.
- [47] Soloiu V, Lewis J, Yoshihara Y, Nishiwaki K. Combustion characteristics of a charcoal slurry in a direct injection diesel engine and the impact on the injection system performance. *Energy* 2011;36(7):4353–71.
- [48] Annand WJD, Ma TH. Instantaneous heat transfer rates to the cylinder head surface of a small compression-ignition engine. In: Proceedings of the Institution of Mechanical Engineers; 1971. p. 976–87.
- [49] Choi B, Jiang X, Kim YK, Jung G, Lee C, Choi I, Song CS. Effect of diesel fuel blend with n-butanol on the emission of a turbocharged common rail direct injection diesel engine. *Appl Energy* 2015;146:20–8.